LETTER

Colossal barocaloric effects in plastic crystals

Bing Li[1]*, Yukinobu Kawakita[2], Seiko Ohira-Kawamura[2], Takeshi Sugahara[3], Hui Wang[4,5], Jingfan Wang[6], Yanna Chen[7], Saori I. Kawaguchi[8], Shogo Kawaguchi[8], Koji Ohara[8], Kuo Li[9], Dehong Yu[10], Richard Mole[10], Takanori Hattori[2], Tatsuya Kikuchi[2], Shin-ichiro Yano[11], Zhao Zhang[1,12], Zhe Zhang[1,12], Weijun Ren[1], Shangchao Lin[6,13], Osami Sakata[7], Kenji Nakajima[2] & Zhidong Zhang[1]

Refrigeration is of vital importance for modern society—for example, for food storage and air conditioning—and 25 to 30 per cent of the world's electricity is consumed for refrigeration[1]. Current refrigeration technology mostly involves the conventional vapour compression cycle, but the materials used in this technology are of growing environmental concern because of their large global warming potential[2]. As a promising alternative, refrigeration technologies based on solid-state caloric effects have been attracting attention in recent decades[3–5]. However, their application is restricted by the limited performance of current caloric materials, owing to small isothermal entropy changes and large driving magnetic fields. Here we report colossal barocaloric effects (CBCEs) (barocaloric effects are cooling effects of pressure-induced phase transitions) in a class of disordered solids called plastic crystals. The obtained entropy changes in a representative plastic crystal, neopentylglycol, are about 389 joules per kilogram per kelvin near room temperature. Pressure-dependent neutron scattering measurements reveal that CBCEs in plastic crystals can be attributed to the combination of extensive molecular orientational disorder, giant compressibility and highly anharmonic lattice dynamics of these materials. Our study establishes the microscopic mechanism of CBCEs in plastic crystals and paves the way to next-generation solid-state refrigeration technologies.

Caloric effects are phase-transition thermal effects regulated by external fields. Large isothermal entropy changes and adiabatic temperature changes are the most important requirements for a caloric material. In the vicinity of a ferromagnetic-to-paramagnetic transition, an applied magnetic field can effectively suppress the disorder of magnetic moments, which in turn accounts for the entropy changes—this is widely known as the magnetocaloric effect (MCE)[3]. Similarly, an electrocaloric effect (ECE) can be also found near a ferroelectric-to-paraelectric transition owing to the alignment of polarizations by electric fields[4]. When magnetic moments (polarizations) are strongly coupled with the lattice degree of freedom, the MCE (ECE) might be enhanced by the change of vibrational entropies[6,7]. In some elastically active compounds known as ferroelastics, an external compressive or tensile stress can also induce a modification of the crystal structure, which brings out the elastocaloric effect[5]. Unlike the three aforementioned caloric effects that are observed in ferroics, the barocaloric effect (BCE) is not system-selective and can in principle be achieved in any atomic system by applying hydrostatic pressure, because pressure is always factored in the free energy of a system. For instance, the BCE was predicted to occur in a few ionic conductors[8] and was later observed[9] in AgI. In addition, a giant BCE has been reported for natural rubber[10]. In this sense, the BCE is the most universal among these solid-state caloric effects.

However, caloric effects of current leading materials are characteristic of entropy changes of dozens of joules per kilogram per kelvin[3–5]. Thus, it is essential to enhance caloric effects by optimizing the working materials. Here we find that plastic crystals are promising next-generation BCE materials, with colossal entropy changes driven by relatively smaller pressures.

Plastic crystals (also termed 'orientation-disordered crystals') are a class of highly disordered solids[11] in which organic molecules (sometimes also inorganic structural blocks) are oriented randomly while their mass centres form highly symmetric lattices, such as the face-centred-cubic (fcc) structure. Upon cooling, the molecules exhibit
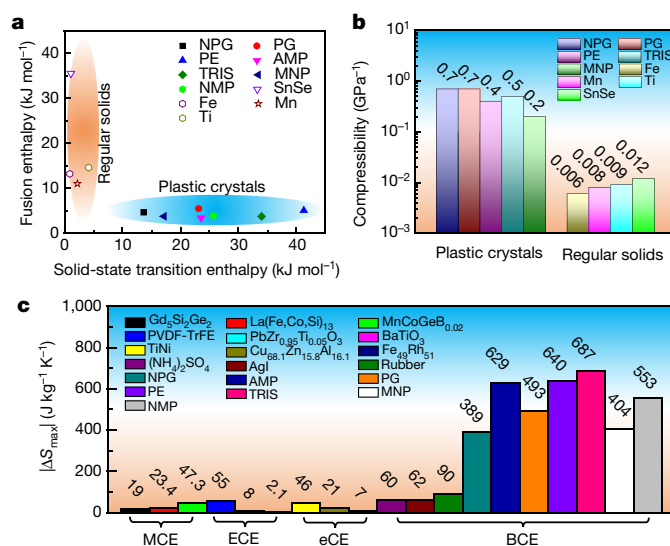
Fig. 1 | Plastic crystals with CBCE for next-generation solid-state refrigeration technology. a, Fusion enthalpy and solid-state transition enthalpy for typical regular solids and plastic crystals: NPG, pentaglycerin (PG), pentaerythritol (PE), AMP, tris(hydroxymethyl)aminomethane (TRIS), 2-methyl-2-nitro-1-propanol (MNP), 2-nitro-2-methyl-1,3-propanediol (NMP)[12–18]. **b**, Compressibility of typical regular solids and plastic crystals[20–22]. **c**, Absolute values of maximum entropy changes, $|\Delta S_{max}|$, for leading caloric materials[3–5,24–29]. The values for plastic crystals are calculated using the Clausius–Clapeyron relation (Extended Data Table 1; in Extended Data Table 2 the entropy changes are also given in J cm^{-3} K^{-1} for reference). For NPG, the directly measured value is shown in Fig. 4b. The background shading indicates the regions in which values for plastic crystals (blue) and regular solids (orange) are found. eCE, elastocaloric effect; PVDF-TrFE, poly(vinylidene fluoride-co-trifluoroethylene).

[1]Shenyang National Laboratory (SYNL) for Materials Science, Institute of Metal Research, Chinese Academy of Sciences, Shenyang, China. [2]J-PARC Center, Japan Atomic Energy Agency, Tokai, Japan. [3]Division of Chemical Engineering, Department of Materials Engineering Science, Graduate School of Engineering Science, Osaka University, Osaka, Japan. [4]Department of Physics and Astronomy, University of California, Irvine, CA, USA. [5]Hunan Key Laboratory of Super Microstructure and Ultrafast Process, School of Physics and Electronics, Central South University, Changsha, China. [6]Department of Mechanical Engineering, Materials Science and Engineering Program, FAMU-FSU College of Engineering, Florida State University, Tallahassee, FL, USA. [7]Synchrotron X-ray Group, Research Center for Advanced Measurement and Characterization, National Institute for Materials Science (NIMS), Sayo, Japan. [8]SPring-8, Japan Synchrotron Radiation Research Institute, Sayo, Japan. [9]Center for High Pressure Science and Technology Advanced Research, Beijing, China. [10]Australian Nuclear Science and Technology Organization (ANSTO), Lucas Heights, New South Wales, Australia. [11]National Synchrotron Radiation Research Center, Hsinchu, Taiwan. [12]School of Materials Science and Engineering, University of Science and Technology of China, Hefei, China. [13]School of Mechanical and Power Engineering, Shanghai Jiao Tong University, Shanghai, China. *e-mail: bingli@imr.ac.cn
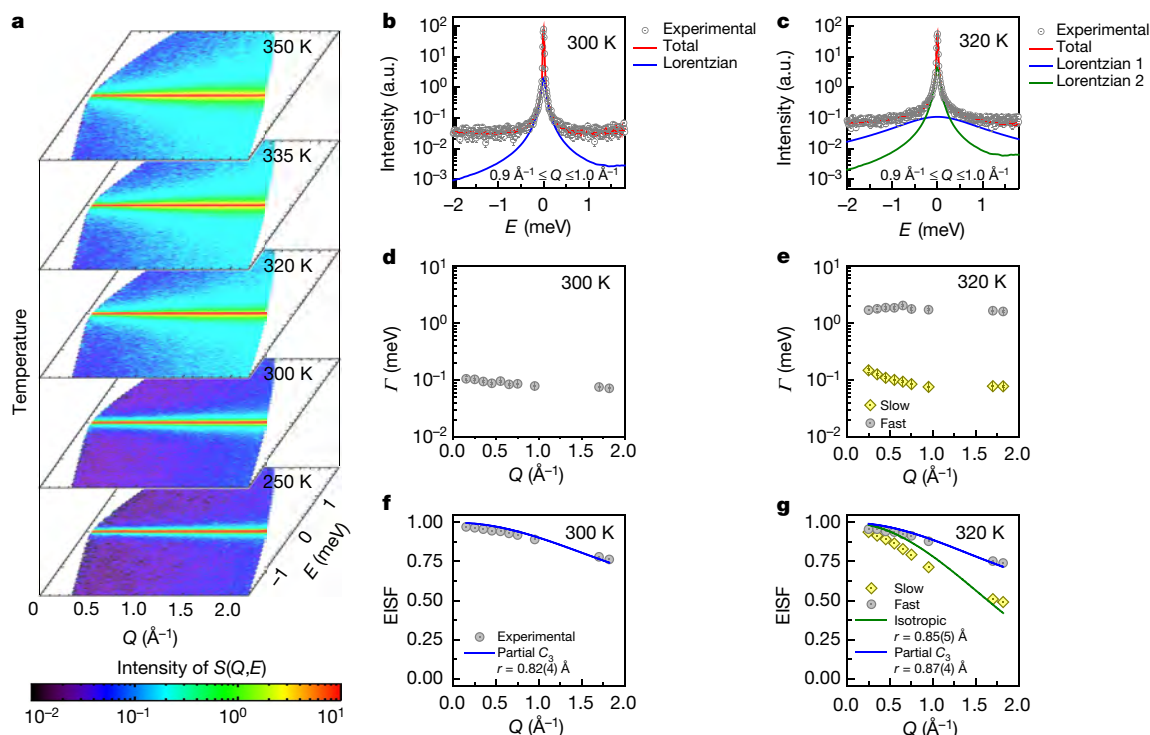
Fig. 2 | Reorientational dynamics of NPG molecules. a, Contour plots of $S(Q, E)$ at five temperatures around T_t, obtained with $E_i = 2.64$ meV at AMATERAS. **b, c**, Incoherent scattering profiles as a function of E at 0.9 Å$^{-1} \leq Q \leq 1.0$ Å^{-1} at 300 K (**b**) and 320 K (**c**). The multiple-component fitting is also shown. One Lorentzian function is needed at 300 K. However, two Lorentzians are involved at 320 K, with Lorentzian 1 being wider (fast motion) than Lorentzian 2 (slow motion). **d, e**, Linewidth at 300 K (**d**) and 320 K (**e**). **f, g**, The EISF at 300 K (**f**) and 320 K (**g**), determined by repeating the fitting at different Q positions using the partial C_3 model and the isotropic reorientational model. r, rotational radius; a.u., arbitrary units.

preferred orientations, which results in a disorder-to-order transition with lattice symmetry breaking. Together with these transitions, huge entropy and/or enthalpy changes are obtained because of the removal of the degeneracy of the many accessible configurations in the disordered state. Owing to this feature, plastic crystals have been used as solid-state thermal energy storage materials[11,12]. As shown in Fig. 1a, their enthalpy changes during solid-state transitions from the ordered state to the plastic phase are substantially larger than fusion enthalpies[12–14], in sharp contrast to regular solids, such as Fe (ref. [15]), Mn (ref. [16]), Ti (ref. [17]) and SnSe (ref. [18]). This means that most of the heat stored in plastic crystals is released during solid-state transitions rather than during melting.

CBCEs can be expected in plastic crystals if disorder-to-order phase transitions can be induced by pressure. Thus, high sensitivity to the applied pressure is a prerequisite for CBCEs, which means that a tiny pressure is able to induce a huge lattice contraction. As implied by their name[19], plastic crystals are usually soft and easily deformed owing to their large compressibility, which is inversely proportional to their density and the square of the speed of sound. We compare the compressibility of leading plastic crystals with that of regular solids[20–22] in Fig. 1b. It can be seen that the former is almost two orders of magnitudes larger than the latter.

The direct lattice effect induced by pressure is translated into entropy changes through dP/dT according to the Clausius–Clapeyron relation[5], where P is the pressure and T is the temperature. For a given system, dP/dT is proportional to the Grüneisen parameter[23] γ, which is a measure of how anharmonic a system is—hence, the more anharmonic a system, the larger the entropy changes obtained. Large anharmonicity is usually found in plastic crystals because they have giant thermal expansion coefficients[20].

Consequently, the combination of extensive disorder, giant compressibility and strong anharmonicity makes plastic crystals ideal hosts for the BCE. As shown in Fig. 1c, colossal entropy changes of around

629 J kg^{-1} K^{-1} at about 350 K in 2-amino-2-methyl-1,3-propanediol (AMP) and of 389 J kg^{-1} K^{-1} in neopentylglycol (NPG) at around room temperature can be obtained—these entropy changes are almost ten times larger than those observed in leading caloric materials so far[3–5,24–29]. Focusing on the representative plastic crystal NPG, we utilize synchrotron X-ray diffraction (XRD), high-resolution quasi-elastic neutron scattering (QENS) and inelastic neutron scattering (INS) techniques to establish the microscopic mechanism of CBCE in plastic crystals.

The molecular configuration of NPG is characteristic of a tetrahedral motif[30], as shown in the inset of Extended Data Fig. 1b. The five carbon atoms form a tetrahedron, in which two carbon atoms are attached to hydrogen atoms in the methyl group, whereas two others form the hydroxymethyl group. At room temperature, the NPG molecules are ordered on a monoclinic lattice with space group $P2_1/n$. This ordered phase transforms into an fcc lattice at $T_t \approx 314$ K on heating. Such a structural transition is evidenced by both elastic neutron scattering and synchrotron XRD measurements (Extended Data Fig. 1) and is coupled with the hydrogen atoms because the incoherent scattering intensity shows an upturn at T_t (Extended Data Fig. 1b).

Next, we move to the dynamic aspects of this compound. In an INS spectrum expressed as a function of energy transfer (E), the peak centred at $E = 0$ represents the elastic information from the static structure, whereas a few peaks centred at $E \neq 0$ represent inelastic scattering originating from excitations such as phonons. In some systems, diffusive and/or reorientational motions lead to QENS, which appears underneath the elastic line. Even though QENS is centred at $E = 0$, similar to the elastic line, it exhibits finite linewidth that is inversely related to the typical time scales of the motions. QENS on a hydrogen-containing molecular system gives direct information on how molecules move. Therefore, we performed QENS measurements on NPG at selected temperatures near T_t. Shown in Fig. 2a are the contour plots of the dynamic structure factor $S(Q, E)$ as a function of momentum transfer (Q) and energy transfer (E) with incident neutron energy
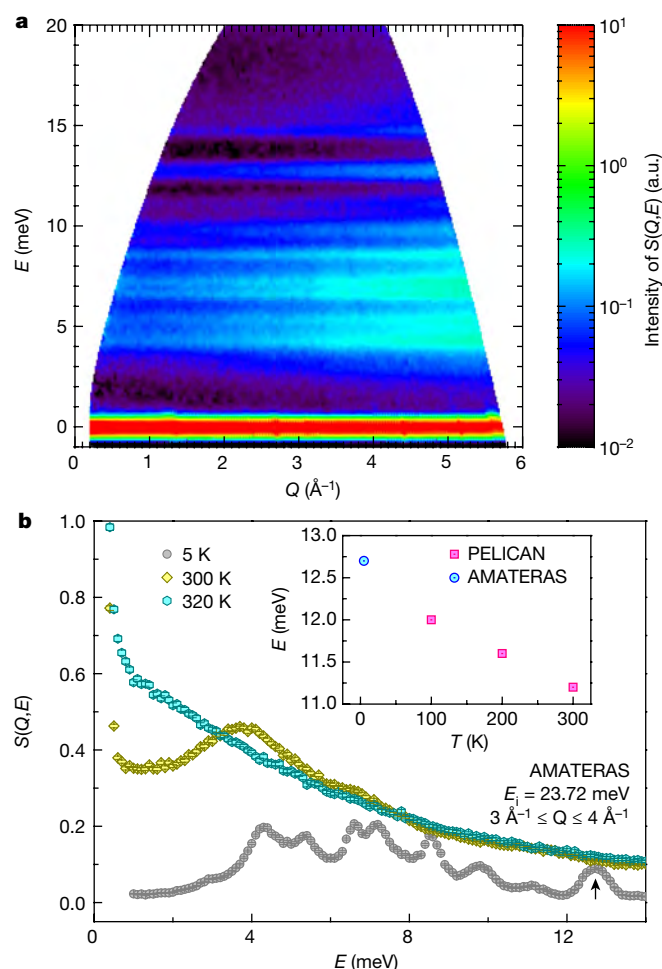
Fig. 3 | Anharmonic lattice dynamics of NPG. a, INS spectrum of NPG at 5 K, obtained with $E_i = 23.72$ meV at AMATERAS. **b**, Sliced $S(Q, E)$ for $0.9\,\text{Å}^{-1} \leq Q \leq 1.0\,\text{Å}^{-1}$ at 5, 300 and 320 K for the AMATERAS data. The inset shows the temperature dependence of the energy of the 12.7-meV mode (shown by the arrow) for the AMATERAS and PELICAN data.

$E_i = 2.64$ meV. The intense stripes centred at $E = 0$ represent the elastic line, which contains most of the scattering intensity. It can be seen that the elastic lines dominate the spectra at 250 K and 300 K. At 320 K, just above T_t, a less-intense signal spreads out from $E = 0$ and weakens as E increases, which corresponds to QENS originating from hydrogen atoms.

At selected Q positions where the Bragg peaks are absent, two-dimensional $S(Q, E)$ data were sliced for QENS fitting (Methods). Shown in Fig. 2b, c are the sliced data for $0.9\,\text{Å}^{-1} \leq Q \leq 1.0\,\text{Å}^{-1}$ at 300 K and 320 K, respectively. The data at 300 K can be well reproduced by a combination of a delta function, a Lorentzian function and a constant background, which are convoluted with the instrumental resolution (Extended Data Fig. 2a). However, an extra Lorentzian function is needed to reproduce the data at 320 K. The linewidth (Γ) of one component is almost 10 times larger than that of another, which means that this motion is much faster. By repeating the fitting at other Q positions, we are able to obtain the intensity of each component and Γ for the Lorentzian function(s). The Q dependences of Γ are summarized in Fig. 2d, e. Both modes exhibit a weak Q dependence, indicating that the associated motions are highly localized. The temperature dependence of Γ for $0.9\,\text{Å}^{-1} \leq Q \leq 1.0\,\text{Å}^{-1}$ above T_t is fitted to the Arrhenius relation and the obtained activation energy E_a is about 47(3) meV (all uncertainties are one standard deviation) for the isotropic reorientational mode (Extended Data Fig. 2d).

On the basis of these results, we introduce the elastic incoherent scattering factor (EISF). The EISF is defined as the ratio between the elastic and the total intensity (Methods), and its Q dependence is directly linked to the nature of the mode. As shown in Fig. 2f, the EISF at 300 K can be well reproduced on the basis of the threefold (C_3) reorientational mode of hydrogen atoms in the methyl groups because the obtained H–H distance in the fitting is 0.82(4) Å (Extended Data Fig. 2e). The EISF for both modes at 320 K is plotted in Fig. 2g. We can see that the EISF of the slow mode decays much more quickly than that of the fast one. The latter is almost identical to the EISF at 300 K, which can also be well reproduced with the partial C_3 model. The slow mode is close to an isotropic reorientational mode with a radius of 0.85(5) Å. This value is approximately equal to the effective distance of the centres of gravity of hydrogen atoms if we simplify the molecular configuration (Extended Data Fig. 2f). Overall, the hydrogen atoms in the methyl group are subjected to C_3 reorientation in both ordered and disordered phases (C_3 reorientation might be further frozen at about 60 K; see Extended Data Fig. 1b), while the whole molecule undergoes isotropic reorientation in the disordered phase.

As we discussed in the beginning, anharmonic lattice dynamics plays a crucial role in BCE. Thus, INS was used to investigate the phonon density of states. Shown in Fig. 3a is the contour plot of $S(Q, E)$ at 5 K for E of up to 20 meV. The figure shows a series of bands centred at $E \neq 0$, which represent optical phonons. The Q-sliced data at $3\,\text{Å}^{-1} \leq Q \leq 4\,\text{Å}^{-1}$ are plotted in Fig. 3b. These phonons appear as well-defined peaks. As the temperature increases, the phonon peaks are gradually broadened and become hardly distinguishable above T_t owing to the molecular orientational disorder (Extended Data Fig. 3). Focusing on the mode at 12.7 meV, which is related to a stretching mode, we track its temperature dependence (inset of Fig. 3b) by combing the AMATERAS and PELICAN data (Extended Data Fig. 3e). It is clear that the mode softens substantially with increasing temperature, which is indicative of giant anharmonicity, given that the microscopic Grüneisen parameter is defined as $-\frac{V}{\omega_i}\frac{\partial \omega_i}{\partial V}$, where V is the volume of a solid and ω_i is the frequency of phonon mode i (ref. [31]).

While the structure and dynamics of the system under ambient pressure are well understood, here we turn to its pressure-dependent properties. Shown in Fig. 4a is a phase diagram determined using high-pressure differential scanning calorimeters (DSCs). There is a thermal hysteresis of about 14 K. As shown in Fig. 4b, for a pressure change from ambient pressure to 91.0 MPa the directly measured entropy change is 384 J kg^{-1} K^{-1}, which is highly consistent with the value of 389 J kg^{-1} K^{-1} estimated using the Clausius–Clapeyron relation (Fig. 1c). This is because the giant compressibility and strong anharmonicity mean that all entropies of the phase transition are released at this pressure. Actually, more than 50% of the maximum entropy changes are achieved at pressures as low as 15.2 MPa, and the entropy changes tend to be saturated at about 45.0 MPa; such low driving pressures are desirable for real applications.

Our synchrotron XRD measurements suggest that the structural phase transition can be induced by a pressure of 200 MPa at 318 K, as shown in Fig. 4c, indicating that the CBCE is related to such a pressure-induced phase transition. More strikingly, the pressure-dependent QENS data directly provide insights into the microscopic dynamics of the system. It can be seen in Fig. 4d, e that the QENS signal, which appears as a trail of the intense elastic line, is mostly suppressed under a pressure of 286 MPa. Indeed, the QENS intensity is already effectively suppressed even at a lower pressure of 178 MPa (Extended Data Fig. 6). These QENS data directly verify that orientational disorder is restrained by the pressure, inducing entropy changes. The pressure suppression of orientational disorder is also manifested in phonons. Shown in Fig. 4f, g are $S(Q, E)$ with $E_i = 23.72$ meV at ambient pressure and at 286 MPa, respectively. It is clear that the phonons centred at about 4 meV become considerably sharper at 286 MPa, which is attributed to the reduced scattering by the orientational disorder. In addition, the pressure effect is demonstrated using molecular dynamics simulations. As shown in Fig. 4h, i, the snapshots of dynamic structures display a transformation
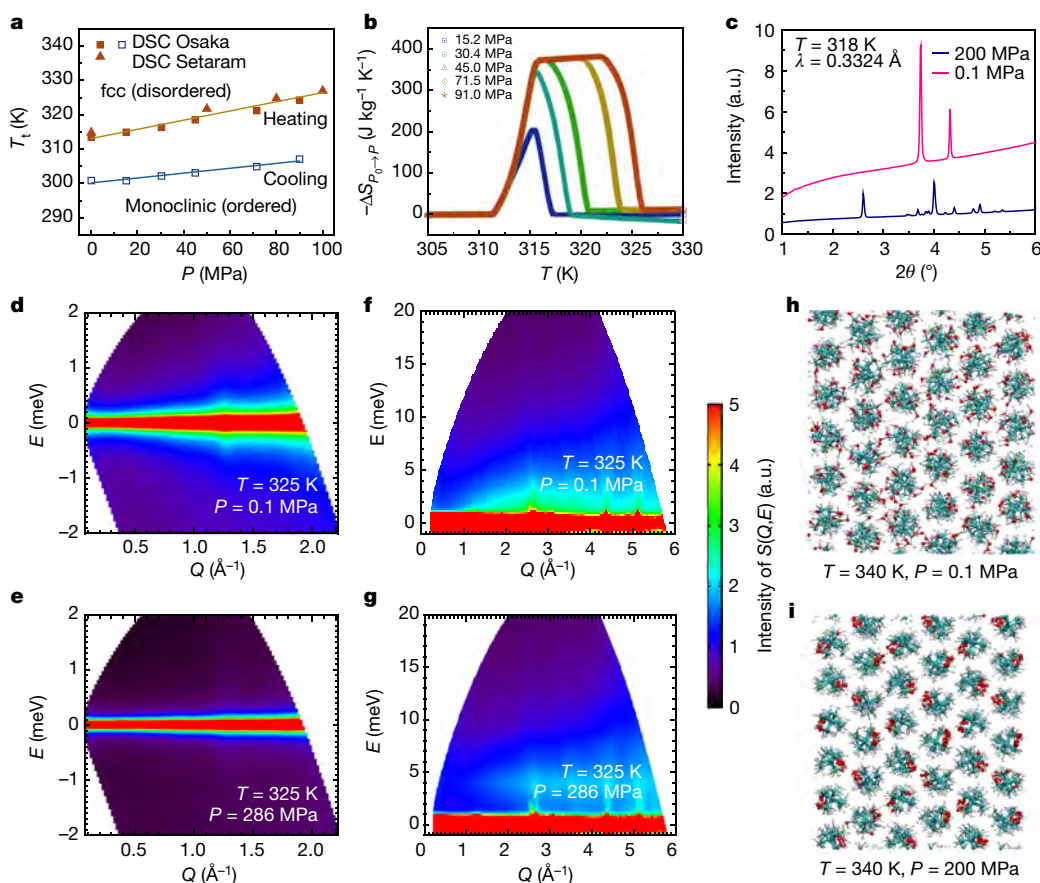
Fig. 4 | Pressure-dependent phase transition and dynamics of NPG.
a, Temperature–pressure phase diagram, determined using high-pressure DSCs. Details about the datasets obtained at Osaka University and at Setaram are provided in Methods. Solid lines are guides for the eye.
b, Pressure-induced entropy changes ($\Delta S_{P_0 \rightarrow P}$) during heating for pressure changes from ambient pressure ($P_0 = 0.1$ MPa) to $P = 15.2$, 30.4, 45.0, 71.5 and 91.0 MPa. **c**, High-pressure synchrotron XRD spectra at 318 K, showing the pressure-induced cubic-to-monoclinic transition. λ, wavelength; θ, scattering angle. **d, e**, QENS measurements at ambient

pressure (**d**) and 286 MPa (**e**), obtained at 325 K with $E_i = 2.64$ meV. **f, g**, INS measurements at ambient pressure (**f**) and 286 MPa (**g**), obtained at 325 K with $E_i = 23.72$ meV. We note that the inelastic signals at about 1.3, 2.6, 4.4 and 5.1 Å^{-1} are contributed by phonons from Teflon (see Methods and Extended Data Figs. 4, 5). **h, i**, Structural snapshots of molecular dynamics simulations at 340 K under ambient pressure (**h**) and 200 MPa (**i**). The red balls represent oxygen atoms, and their random arrangements are suppressed under pressure (for the detailed distribution of orientations, refer to Extended Data Fig. 7).

to ordered arrangements of molecules with increasing pressures of up to 200 MPa. In fact, the disorder is already effectively suppressed at 100 MPa (Extended Data Fig. 7b). These experimental and theoretical insights unambiguously indicate that the CBCE of NPG can be attributed to the suppression of the extensive orientational disorder by pressure.

We have established the microscopic mechanism of CBCEs in plastic crystals by taking NPG as an example. For the practical application of plastic crystals in solid-state refrigeration technologies, two important issues have to be addressed. Even though the estimated adiabatic temperature change is as high as 50 K (Methods), many engineering optimizations are needed to approach this value, such as enhancing thermal conduction and reducing heat dissipation by compositing with thermally conductive materials[32]. Moreover, the drawback of thermal hysteresis could be overcome by creating a reversible refrigeration cycle based on the combination of electric field and pressure, in analogy to MCE[33], given that most molecules of plastic crystals, including NPG, are polar[14].

To summarize, we have discovered that plastic crystals exhibit CBCEs and revealed the microscopic origin through pressure-dependent QENS and INS measurements. Plastic crystals are very promising for practical refrigeration applications given that they are abundantly available, environmentally friendly and easily driven and have high performance. Our work indicates a new direction for emergent solid-state refrigeration technologies.

Online content

Any methods, additional references, Nature Research reporting summaries, source data, statements of data availability and associated accession codes are available at https://doi.org/10.1038/s41586-019-1042-5.

1. United Nations Environment Programme. *The Importance of Energy Efficiency in the Refrigeration, Air-Conditioning and Heat Pump Sectors. Briefing Note A* http://conf.montreal-protocol.org/meeting/workshops/energy-efficiency/presession/breifingnotes/briefingnote-a_importance-of-energy-efficiency-in-the-refrigeration-air-conditioning-and-heat-pump-sectors.pdf (United Nations Environment Programme, May 2018).
2. Molenbroek, E. et al. *Savings and Benefits of Global Regulations for Energy Efficient Products.* Final Report https://ec.europa.eu/energy/sites/ener/files/documents/Cost%20of%20Non-World%20-%20Final%20Report.pdf (European Commission, 2015).
3. Shen, B. G., Sun, J. R., Hu, F. X., Zhang, H. W. & Cheng, Z. H. Recent progress in exploring magnetocaloric materials. *Adv. Mater.* **21**, 4545–4564 (2009).
4. Scott, J. F. Electrocaloric materials. *Annu. Rev. Mater. Res.* **41**, 229–240 (2011).
5. Mañosa, L. et al. Materials with giant mechanocaloric effects: cooling by strength. *Adv. Mater.* **29**, 1603607 (2017).
6. Li, B. et al. Magnetostructural coupling and magnetocaloric effect in Ni–Mn–In. *Appl. Phys. Lett.* **95**, 172506 (2009).
7. Li, B. et al. Intrinsic electrocaloric effects in ferroelectric poly(vinylidene fluoride-trifluoroethylene) copolymers: roles of order of phase transition and stresses. *Appl. Phys. Lett.* **96**, 102903 (2010).
8. Cazorla, C. & Errandonea, D. Giant mechanocaloric effects in fluorite-structured superionic materials. *Nano Lett.* **16**, 3124–3129 (2016).

9. Aznar, A. et al. Giant barocaloric effects over a wide temperature range in superionic conductor AgI. *Nat. Commun.* **8**, 1851 (2017).
10. Bom, N. M. et al. Giant barocaloric effects in natural rubber: a relevant step toward solid-state cooling. *ACS Macro Lett.* **7**, 31–36 (2018).
11. Parsonage, N. G. & Staveley, L. A. K. *Disorder in Crystals* (Clarendon Press, Oxford, 1979).
12. Chandra, D. et al. Phase transitions in "plastic crystals". *J. Less Common Met.* **168**, 159–167 (1991).
13. Murrill, E. et al. Solid–solid phase transitions determined by differential scanning calorimetry: part I. Tetrahedral substances. *Thermochim. Acta* **1**, 239–246 (1970).
14. Tamarit, J. L. et al. Dielectric studies on orientationally disordered phases of neopentylglycol ((CH_3)$_2$C(CH_2OH)$_2$) and tris(hydroxymethyl aminomethane) ((NH_2)C(CH_2OH)$_3$). *J. Phys. Condens. Matter* **9**, 5469–5478 (1997).
15. Desai, P. D. Thermodynamic properties of iron and silicon. *J. Phys. Chem. Ref. Data* **15**, 967–983 (1986).
16. Desai, P. D. Thermodynamic properties of manganese and molybdenum. *J. Phys. Chem. Ref. Data* **16**, 91–108 (1987).
17. Desai, P. D. Thermodynamic properties of titanium. *Int. J. Thermophys.* **8**, 781–794 (1987).
18. Yamaguchi, K. et al. Measurements of high temperature heat content of the II–VI and IV–VI (II: Zn, Cd IV: Sn, Pb VI: Se, Te) compounds. *Mater. Trans.* **35**, 118–124 (1994).
19. Timmermans, J. Un nouvel état mésomorphe les cristaux organiques plastiques. *J. Chim. Phys.* **35**, 331–344 (1938).
20. Font, J. et al. Plastic crystals: dilatometric and thermobarometric complementary studies. *Mater. Res. Bull.* **30**, 839–844 (1995).
21. *Webelements* http://www.webelements.com/.
22. Bansal, D. et al. Phonon anharmonicity and negative thermal expansion in SnSe. *Phys. Rev. B* **94**, 054307 (2016).
23. Hanneman, R. E. et al. Relationship between compressibility and thermal expansion coefficients in cubic metals and alloys. *J. Appl. Phys.* **36**, 1794–1796 (1965); erratum **38**, 1988 (1967).
24. Mañosa, L. et al. Giant solid-state barocaloric effect in the Ni–Mn–In magnetic shape-memory alloy. *Nat. Mater.* **9**, 478–481 (2010).
25. Lloveras, P. et al. Giant barocaloric effects at low pressure in ferrielectric ammonium sulphate. *Nat. Commun.* **6**, 8801 (2015).
26. Bermúdez-García, J. M. et al. Giant barocaloric effect in the ferroic organic-inorganic hybrid [TPrA][Mn(dca)$_3$] perovskite under easily accessible pressures. *Nat. Commun.* **8**, 15715 (2017).
27. Trung, N. T., Zhang, L., Caron, L., Buschow, K. H. J. & Brück, E. Giant magnetocaloric effects by tailoring the phase transitions. *Appl. Phys. Lett.* **96**, 172504 (2010).
28. Lu, S. G. et al. Comparison of directly and indirectly measured electrocaloric effect in relaxor ferroelectric polymers. *Appl. Phys. Lett.* **97**, 202901 (2010).
29. Cui, J. et al. Demonstration of high efficiency elastocaloric cooling with large ΔT using NiTi wires. *Appl. Phys. Lett.* **101**, 073904 (2012).
30. Chandra, D. et al. Low- and high-temperature structures of neopentylglycol plastic crystal. *Powder Diffr.* **8**, 109–117 (1993).
31. Grüneisen, E. Theorie des festen zustandes einatomiger elemente. *Ann. Phys.* **344**, 257–306 (1912).
32. Wang, X., Guo, Q., Zhong, Y., Wei, X. & Liu, L. Heat transfer enhancement of neopentyl glycol using compressed expanded natural graphite for thermal energy storage. *Renew. Energy* **51**, 241–246 (2013).
33. Stern-Taulats, E. et al. Caloric effects in ferroic materials. *MRS Bull.* **43**, 295–299 (2018).

Author contributions B.L. and Zhidong Zhang conceived the idea. B.L., Y.K., T.K., S.O.-K., T.H. and K.N. performed the neutron scattering experiments at AMATERAS. T.H. calibrated the pressures at PLANET. S.-i.Y. collected the elastic data at SIKA. D.Y. and R.M. conducted the INS measurements at PELICAN. B.L., Y.C., S.I.K., K.O., S.K. and O.S. carried out synchrotron XRD measurements. K.L. analysed the XRD data. T.S. performed pressure-dependent DSC characterizations. H.W. calculated the vibrational spectra. J.W. and S.L. conducted the molecular dynamics simulations. Zhao Zhang, Zhe Zhang and W.R. carried out the in-house XRD and DSC measurements under ambient pressure for testing the samples. B.L. analysed neutron data and wrote the manuscript with discussion and input from all coauthors.

METHODS

Sample. A powder sample of NPG (IUPAC name: 2,2-dimethyl-1,3-propanediol) with 99% purity was purchased from Sigma-Aldrich. The as-received powder was checked using an in-house X-ray diffractometer (D8 Advance, Bruker) and a DSC (Q1000, TA Instruments).

High-pressure calorimetric measurements. Heat flow data were collected using the DSC μDSC 7 EVO at Osaka University, Japan at 0.1, 15.2, 30.4, 45.0, 71.5 and 91.0 MPa (Fig. 4b) and at Setaram, France at 0.1, 50, 80 and 100 MPa (Extended Data Fig. 6d). The samples were capsuled in high-pressure vessels and the required pressures were generated through high-pressure nitrogen gas controlled by a high-pressure gas panel. The scanning rate was 0.1 K min^{-1}. The phase-transition temperature was defined as the temperature at which the heat flow peaked. The entropy changes under constant pressures were calculated by integrating the heat flow $Q(P, T)$, after subtracting the baseline, in the temperature interval between T_1 and T_2,

$$\Delta S_P = \int_{T_1}^{T_2} \frac{1}{T} \frac{Q(P, T)}{T'} dT \tag{1}$$

where T' is the temperature ramping rate[24,34]. Hence, the pressure-induced entropy changes for the pressure change from the ambient (P_0) to the applied pressure (P) were calculated as

$$\Delta S_{P_0 \to P} = \Delta S_P - \Delta S_{P_0} \tag{2}$$

The obtained entropy changes allowed us to estimate the adiabatic temperature changes. A previous study suggested that the specific heat near the phase transition is about 250 J mol^{-1} K^{-1} (off the peak)[35], which only accounts for about 50% of the $3R$ value determined by the Dulong–Petit law (where R is the gas constant, and $3R$ is the upper limit on the specific heat of a solid according to the Dulong–Petit law). This is because the frequencies of most vibrational modes are higher than 30 meV, as suggested by density functional theory (DFT) calculations (Extended Data Fig. 7c), so many modes are not excited at room temperature and the specific heat is not saturated. It is known that the lattice of a caloric material acts also as the thermal loading in a refrigeration cycle, so a system with fewer atoms in the unit cell is desirable for efficient refrigeration application. Even though a plastic crystal may consist of very complex molecules, excellent caloric performance is guaranteed by the unique lattice dynamics. By taking the specific heat, we estimate that the maximum adiabatic temperature changes[34] are as high as 50 K.

Synchrotron XRD. Synchrotron XRD measurements were performed at the high-resolution X-ray diffractometer BL02B2 of SPring-8 in Japan using a powder sample of NPG sealed in a capillary under ambient pressure[36]. The wavelength was 0.9994 Å. The sample was heated from 273 K to 353 K, with 10 K as the step, and a constant-temperature scan was carried out for 30 s. The diffraction data were analysed using Jana 2006[37] and a monoclinic model for the low-temperature phase[30]. The lattice constants of the high-temperature phase were calculated using the Bragg peaks of (111) and (200). The high-pressure synchrotron XRD data were collected at the high-energy X-ray diffractometer BL04B2 of SPring-8 using a diamond anvil cell[38]. The pressure was determined using a ruby pressure scale at a wavelength of 0.3324 Å.

Elastic neutron scattering at SIKA. The neutron scattering measurement was performed with the cold-neutron triple-axis spectrometer SIKA at the Australian Center for Neutron Scattering (ACNS) of the Australian Nuclear Science and Technology (ANSTO) facility in Australia[39]. About 6.6 g of NPG powder was sealed into an aluminium can under helium gas. The incident (E_i) and final (E_f) neutron energies were fixed at 5.0 meV to achieve elastic scattering intensities. The monochromator was vertically focused. Collimations were set to be open–open 60′–60′. A cooled Be filter was placed on the scattering side of SIKA to cut off higher-order contamination (such as $\lambda/2$ and $\lambda/3$, where λ is the neutron wavelength). Constant-Q scans were made at 2.1 Å^{-1} to obtain the incoherent elastic neutron scattering intensities.

QENS/INS at AMATERAS. Multi-incident-energy (E_i) time-of-flight INS measurements were performed at the cold-neutron disk-chopper spectrometer BL14 AMATERAS of J-PARC in Japan[40,41]. A powder sample of around 0.29 g was wrapped with aluminium foil and further sealed into an aluminium can with indium wire. Such a geometry ensures about 80% transmission of neutrons, which is crucial for obtaining high-quality QENS data. A cryostat was used to access a broad temperature region. The chopper configurations were 300 Hz (CH01), 300 Hz (CH02) with a slit width of 10 mm, and 150 Hz (CH03), which enabled the selection of E_i = 23.72, 5.93, 2.64 meV with superior energy resolution of 0.42, 0.078, and 0.026 meV, respectively, as shown in Extended Data Fig. 2. The data reduction was performed using the Utsusemi suite[42]. The resulting $S(Q, E)$ data were visualized in Mslice of DAVE[43]. The contour plots of $S(Q, E)$ with E_i of 23.72 meV and 5.93 meV are shown in Extended Data Fig. 3.

The high-pressure INS data were collected with the same E_i but with a slit size of 30 mm to enhance the intensity, using a clamped cell made of an Al–Zn–Mg-based

alloy (Mesoalite)[44]. The powder sample was mixed with reagent-grade KBr powder (Kanto Chemical) to reduce multiple scattering and to ensure quasi-hydrostatic conditions. We note that KBr has very limited incoherent scattering length, which is very important for QENS measurements. A mixture of the sample and KBr powder at a volumetric ratio of 1:1 was used to fabricate a pellet of 6.5 mm diameter and 22.5 mm length, which was inserted into a sample cell made of Teflon. The sample was compressed to the desirable loading with a hand press, using a load–pressure curve determined beforehand. The actual pressure generated in the cell was determined at the high-pressure neutron diffractometer (PLANET) of J-PARC[45] from the change of the lattice parameters of KBr using the equation of state[46]. We note that the inelastic signals at about 1.3, 2.6, 4.4 and 5.1 Å^{-1} in Fig. 4d–g are contributed by phonons from the Teflon (see Extended Data Figs. 4, 5 for details).

INS at PELICAN. The INS experiment was performed using the cold-neutron time-of-flight spectrometer PELICAN at the ACNS of ANSTO in Australia[47,48]. The instrument was configured for incident neutrons with a wavelength of 5.96 Å, affording an energy resolution of 0.065 meV at the elastic line for this experiment. A powder sample of NPG was loaded into a flat-plate aluminium can with a sample thickness of 0.2 mm under dry nitrogen gas environment. The sample was oriented at 135° to the incident neutron beam. A top-loading cryostat was used to maintain the sample temperature from 10 K to 350 K. A background spectrum (for an empty can) and the instrument resolution function (from a standard vanadium sample) were collected under the same configuration as the sample measurements. The spectrum of the vanadium standard was also used for detector normalization. All data reduction and manipulation, including background subtraction and detector normalization, were done using the Large Array Manipulation Program (LAMP)[49]. The general density of state is shown in Extended Data Fig. 3.

QENS analysis and reorientational dynamics. The supreme energy resolution for E_i = 2.64 meV at AMATERAS allowed us to thoroughly examine the QENS information. The $S(Q, E)$ data were converted into one-dimensional data at specific Q points. Q-slicing was done using the energy intervals [0.1 Å^{-1},0.2 Å^{-1}], [0.2 Å^{-1},0.3 Å^{-1}], [0.3 Å^{-1},0.4 Å^{-1}], [0.4 Å^{-1},0.5 Å^{-1}], [0.5 Å^{-1},0.6 Å^{-1}], [0.6 Å^{-1},0.7 Å^{-1}], [0.7 Å^{-1},0.8 Å^{-1}] [0.9 Å^{-1},1.0 Å^{-1}], [1.65 Å^{-1},1.75 Å^{-1}] and [1.78 Å^{-1},1.88 Å^{-1}]. These spectra were fitted using the PAN module of DAVE by including one Lorentzian function below T_t and two Lorentzians above T_t, a delta function and a constant background, which were convoluted to the instrumental resolution and described the quasi-elastic scattering, incoherent elastic scattering and background, respectively. The 5-K data were used as resolution functions for the individual Q position.

At 300 K, only one Lorentzian function is needed, with an EISF defined by the intensity ratio[50]

$$\text{EISF}(300\text{ K}) = \frac{I_{\text{elastic}}}{I_{\text{elastic}} + I_{\text{QENS}}} \tag{3}$$

Because there are two Lorentzian functions at 320 K, this definition is modified as

$$\text{EISF}(320\text{ K, slow}) = \frac{I_{\text{elastic}}}{I_{\text{elastic}} + I_{\text{QENS,slow}}} \tag{4}$$

$$\text{EISF}(320\text{ K, fast}) = \frac{I_{\text{elastic}} + I_{\text{QENS,slow}}}{I_{\text{elastic}} + I_{\text{QENS,slow}} + I_{\text{QENS,fast}}} \tag{5}$$

The EISF at 300 K is well reproduced by the partial threefold (C_3) reorientational modes of the hydrogen atoms in the methyl group, given as[51]

$$\text{EISF(partial } C_3) = \frac{1}{2} + \frac{1}{2} \times \frac{1}{3}\left[1 + \frac{2\sin(\sqrt{3}\,Qr)}{\sqrt{3}\,Qr}\right] \tag{6}$$

Here, r is the radius of the circle on which the hydrogen atoms rotate. The fitted value is 0.82(4) Å, which is close to the crystallographic data. At 320 K, the EISF of the fast mode can also be fitted with this model, resulting in a value of 0.87(4) Å, whereas the slow mode can be reproduced using the isotropic rotation model, with the EISF given as[50]

$$\text{EISF(isotropic)} = \left[\frac{\sin(Qr)}{Qr}\right]^2 \tag{7}$$

The resulting r is 0.85(5) Å, which approximates the configuration in which the centre of gravity of the incoherent scattering objects is on the carbon atoms that lie on the corners of the tetrahedron, as shown in Extended Data Fig. 2. The interplay between the reorientational modes and phonons is described in Extended Data Fig. 3, where it can be seen that the phonons become over-broadened as the isotropic reorientational modes of the molecules are activated above T_t.

Molecular dynamics simulations. All-atomistic molecular dynamics simulations of crystalline NPG systems were carried out using the LAMMPS[52]

package to investigate the phase-transition processes. To describe the plastic crystal structure of NPG, the OPLS-AA force field[53] was used. A time step of 1 fs and a cutoff distance of 1 nm for the short-range Lennard-Jones and Coulomb electrostatic interactions were chosen. In addition, the particle-mesh Ewald summation method[54] was used here to treat long-range electrostatic interactions beyond the cutoff. Three-dimensional periodic boundary conditions were applied to all the simulations. An initial NPG crystal structure in a triclinic (non-orthogonal) simulation box, which was used in all the molecular dynamics simulations, was created based on DFT calculations. The initial system included 216 NPG molecules and the simulation box had initial dimensions of about $3.59 \times 3.26 \times 2.99$ nm^3 (along the X, Y and Z directions) and a tilting factor of around -0.51 nm (with respect to the X–Z plane). After energy minimization, systems were simulated using the NPT ensemble under various conditions for 10 ns using the Nosé–Hoover[55,56] barostat and thermostat. The controlled temperatures were in the range 325–355 K. The normal stresses along the X, Y and Z directions were controlled independently at 0.1 (ambient pressure), 100 and 200 MPa, whereas the shear stresses along the X–Y, X–Z and Y–Z planes were kept at zero for all molecular dynamics simulations. After equilibrating the NPG systems under various temperature (325–355 K) and pressure (0.1, 100 and 200 MPa) combinations, the final molecular dynamics simulation snapshots were analysed to identify the phase-transition temperatures through the computed structural features (that is, the NPG molecular orientations).

DFT calculations. The DFT calculations were performed with VASP (Vienna ab initio simulation package)[57,58]. The spin-polarized generalized gradient approximation[59] was used for the description of the exchange-correlation interaction among electrons. We treated C-$2s2p$, H-$1s$ and O-$2s2p$ as valence states and adopted the projector-augmented wave pseudopotentials to represent the effect of their ionic cores[60,61]. Spin–orbit coupling was not included in the calculation because spin–orbit coupling of C, H and O is very weak. We sampled the Brillouin zone by adopting the Γ-centred Monkhorst–Pack[62] method with a density of about $2\pi \times 0.03$ Å^{-1} in all calculations. Brillouin zone integrations were performed with a Gaussian broadening of 0.05 eV during all calculations[63]. For the correct description of the weak interaction between molecules, the non-local van der Waals correction was included using the DFT-D3 method[64]. Finite differences were used to obtain the forces by displacing each ion in three Cartesian directions, from which the Hessian matrix and vibrational frequencies were determined. The energy cutoff for the plane-wave expansion was 600 eV, which resulted in good convergence of the computed ground-state properties. Structures were optimized with the criterion that the atomic force on each atom was weaker than 0.01 eV Å^{-1} and the energy convergence was better than 10^{-6} eV. The obtained lattice parameters are compared with the experimental ones in Extended Data Table 3. The obtained vibrational spectra are plotted in Extended Data Fig. 7c.

Data availability

The data that support the findings of this study are available from the corresponding author upon reasonable request.

34. Moya, X. et al. Caloric materials near ferroic phase transitions. *Nat. Mater.* **13**, 439–450 (2014).
35. Chandra, D. et al. Heat capacities of "plastic crystal" solid state thermal energy storage materials. *Z. Phys. Chem.* **216**, 1433 (2002).
36. Kawaguchi, S. et al. High-throughput powder diffraction measurement system consisting of multiple MYTHEN detectors at beamline BL02B2 of SPring-8. *Rev. Sci. Instrum.* **88**, 085111 (2017).
37. Petříček, V., Dušek, M. & Palatinus, L. Crystallographic computing system JANA2006: general features. *Z. Kristallogr.* **229**, 345–352 (2014).
38. Isshiki, M., Ohishi, Y., Goto, S., Takeshita, K. & Ishikawa, T. High-energy X-ray diffraction beamline: BL04B2 at SPring-8. *Nucl. Instrum. Meth. Phys. Res. B* **467–468**, 663–666 (2001).
39. Wu, C.-M. et al. SIKA–the multiplexing cold-neutron triple-axis spectrometer at ANSTO. *J. Inst.* **11**, P10009 (2016).
40. Nakajima, K. et al. AMATERAS: a cold-neutron disk chopper spectrometer. *J. Phys. Soc. Jpn* **80**, SB028 (2011).
41. Nakamura, M. et al. First demonstration of novel method for inelastic neutron scattering measurement utilizing multiple incident energies. *J. Phys. Soc. Jpn* **78**, 093002 (2009).
42. Inamura, Y. et al. Development status of software "Utsusemi" for chopper spectrometers at MLF, J-PARC. *J. Phys. Soc. Jpn* **82**, SA031 (2013).
43. Azuah, R. T. et al. DAVE: a comprehensive software suite for the reduction, visualization, and analysis of low energy neutron spectroscopic data. *J. Res. Natl Inst. Stand. Technol.* **114**, 341–358 (2009).
44. Aso, N., Fujiwara, T., Uwatoko, Y., Miyano, H. & Yoshizawa, H. Development of a hybrid CuBe/NiCrAl clamp-type high pressure cell for neutron diffraction. *J. Phys. Soc. Jpn* **76**, 228–229 (2007).
45. Hattori, T. et al. Design and performance of high-pressure PLANET beamline at pulsed neutron source at J-PARC. *Nucl. Instrum. Methods Phys. Res. A* **780**, 55–67 (2015).
46. Dewaele, A. et al. High-pressure-high-temperature equation of state of KCl and KBr. *Phys. Rev. B* **85**, 214105 (2012).
47. Yu, D. et al. Performance test on PELICAN – a multi-purpose time of flight cold neutron spectrometer. *EPJ Web Conf.* **83**, 03019 (2015).
48. Yu, D. et al. Pelican – a time of flight cold neutron polarization analysis spectrometer at OPAL. *J. Phys. Soc. Jpn* **82**, SA027 (2013).
49. Richard, D. et al. Analysis and visualisation of neutron-scattering data. *J. Neutr. Res.* **4**, 33–39 (1996).
50. Bée, M. *Quasielastic Neutron Scattering Principles and Applications in Solid State Chemistry, Biology and Materials Science* (IOP, Bristol, 1988).
51. Silvi, L., Röhm, E., Fichtner, M., Petry, W. & Lohstroh, W. Hydrogen dynamics in β-Mg(BH$_4$)$_2$ on the picosecond timescale. *Phys. Chem. Chem. Phys.* **18**, 14323–14332 (2016).
52. Plimpton, S. Fast parallel algorithms for short-range molecular dynamics. *J. Comput. Phys.* **117**, 1–19 (1995).
53. Jorgensen, W. L., Maxwell, D. S. & Tirado-Rives, J. Development and testing of the OPLS all-atom force field on conformational energetics and properties of organic liquids. *J. Am. Chem. Soc.* **118**, 11225–11236 (1996).
54. Darden, T., York, D. & Pedersen, L. Particle mesh Ewald: An N·log(N) method for Ewald sums in large systems. *J. Chem. Phys.* **98**, 10089–10092 (1993).
55. Nosé, S. A. A unified formulation of the constant temperature molecular dynamics methods. *J. Chem. Phys.* **81**, 511–519 (1984).
56. Hoover, W. G. Canonical dynamics: equilibrium phase-space distributions. *Phys. Rev. A* **31**, 1695–1697 (1985).
57. Kresse, G. et al. Efficient iterative schemes for ab initio total-energy calculations using a plane-wave basis set. *Phys. Rev. B* **54**, 11169–11186 (1996).
58. Kresse, G. et al. Ab initio molecular-dynamics simulation of the liquid-metal–amorphous-semiconductor transition in germanium. *Phys. Rev. B* **49**, 14251–14269 (1994).
59. Perdew, J. P. et al. Generalized gradient approximation made simple. *Phys. Rev. Lett.* **77**, 3865–3868 (1996); erratum **78**, 1396 (1997).
60. Kresse, G. et al. From ultrasoft pseudopotentials to the projector augmented-wave method. *Phys. Rev. B* **59**, 1758–1775 (1999).
61. Blöchl, P. E. Projector augmented-wave method. *Phys. Rev. B* **50**, 17953–17979 (1994).
62. Monkhorst, H. J. & Pack, J. D. Special points for Brillouin-zone integrations. *Phys. Rev. B* **13**, 5188–5192 (1976).
63. Elsässer, C. et al. Density-functional energies and forces with Gaussian-broadened fractional occupations. *Phys. Rev. B* **49**, 13975–13978 (1994).
64. Grimme, S. et al. A consistent and accurate ab initio parametrization of density functional dispersion correction (DFT-D) for the 94 elements H–Pu. *J. Chem. Phys.* **132**, 154104 (2010).
65. Svitelskiy, O. et al. Elastic properties of Gd$_5$Si$_2$Ge$_2$ studied with an ultrasonic pulse-echo technique. *Phys. Rev. B* **74**, 184105 (2006).
66. Pecharsky, V. K. & Gschneidner, K. A. Jr Giant magnetocaloric effect in Gd$_5$(Si$_2$Ge$_2$). *Phys. Rev. Lett.* **78**, 4494–4497 (1997).
67. Katter, M., Zellmann, V., Reppel, G. W. & Uestuener, K. Magnetocaloric properties of La(Fe,Co,Si)$_{13}$ bulk material prepared by powder metallurgy. *IEEE Trans. Magn.* **44**, 3044 (2008).
68. Kanomata, T. et al. Magneto-volume effect of MnCo$_{1-x}$Ge (0 ≤ x ≤ 0.2). *J. Magn. Magn. Mater.* **140–144**, 131–132 (1995).
69. Oliveira, F. et al. Process influences on the structure, piezoelectric, and gas-barrier properties of PVDF-TrFE copolymer. *J. Polym. Sci. B* **52**, 496–506 (2014).
70. Shkuratov, S. I. et al. Depolarization mechanisms of PbZr$_{0.52}$Ti$_{0.48}$O$_3$ and PbZr$_{0.95}$Ti$_{0.05}$O$_3$ poled ferroelectrics under high strain rate loading. *Appl. Phys. Lett.* **104**, 212901 (2014).
71. Mischenko, A. S., Zhang, Q., Scott, J. F., Whatmore, R. W. & Mathur, N. D. Giant electrocaloric effect in thin-film PbZr$_{0.95}$Ti$_{0.05}$O$_3$. *Science* **311**, 1270–1271 (2006).
72. Buttner, R. & Maslen, E. Structural parameters and electron difference density in BaTiO$_3$. *Acta Crystallogr. B* **48**, 764–769 (1992).
73. Moya, X. et al. Giant electrocaloric strength in single-crystal BaTiO$_3$. *Adv. Mater.* **25**, 1360–1365 (2013).
74. Wang, F. E., Buehler, W. J. & Pickart, S. J. Crystal structure and a unique "martensitic" transition of TiNi. *J. Appl. Phys.* **36**, 3232–3239 (1965).
75. Bonnot, E., Romero, R., Mañosa, Ll., Vives, E. & Planes, A. Elastocaloric effect associated with the martensitic transition in shape-memory alloys. *Phys. Rev. Lett.* **100**, 125901 (2008).
76. Nikitin, S. A. et al. Giant elastocaloric effect in FeRh alloy. *Phys. Lett. A* **171**, 234–236 (1992).
77. Moore, M. J. & Kasper, J. S. Crystal structure of AgI at 3 kbar. *J. Chem. Phys.* **48**, 2446 (1968).
78. Arroyo, M., Lopez-Manchado, M. & Herrero, B. Organo-montmorillonite as substitute of carbon black in natural rubber compounds. *Polymer* **44**, 2447–2453 (2003).
79. Rose, H. A. & Vancamp, A. 2-Amino-2-methyl-1,2-propanediol. *Anal. Chem.* **28**, 1790–1791 (1956).
80. Johnson, D. J., Ervin, J. S., Hanchak, M. & Hu, X. Graphite foam infused with pentaglycerine for solid-state thermal energy storage. *J. Thermophys. Heat Transfer* **29**, 55–64 (2015).
81. Zhurov, V. V., Zhurova, E. A., Chen, Y. S. & Pinkerton, A. A. Accurate charge density data collection in under a day with a home X-ray source. *J. Appl. Crystallogr.* **38**, 827–829 (2005).
82. Kendi, E. Molecular and crystal structure of tris(hydroxymethyl)aminomethane. *Z. Kristallogr.* **160**, 139–143 (1982).
83. Tamarit, J. L. et al. Crystal data of the low-temperature solid form of 2-methyl-2-nitro-propanol. *Powder Diff.* **9**, 84–86 (1994).
84. Marr, H., Kruger, G. & Stewart, J. 2-Methyl-2-nitro-1, 3-propanediol. *Acta Crystallogr. B* **33**, 2886–2887 (1977).
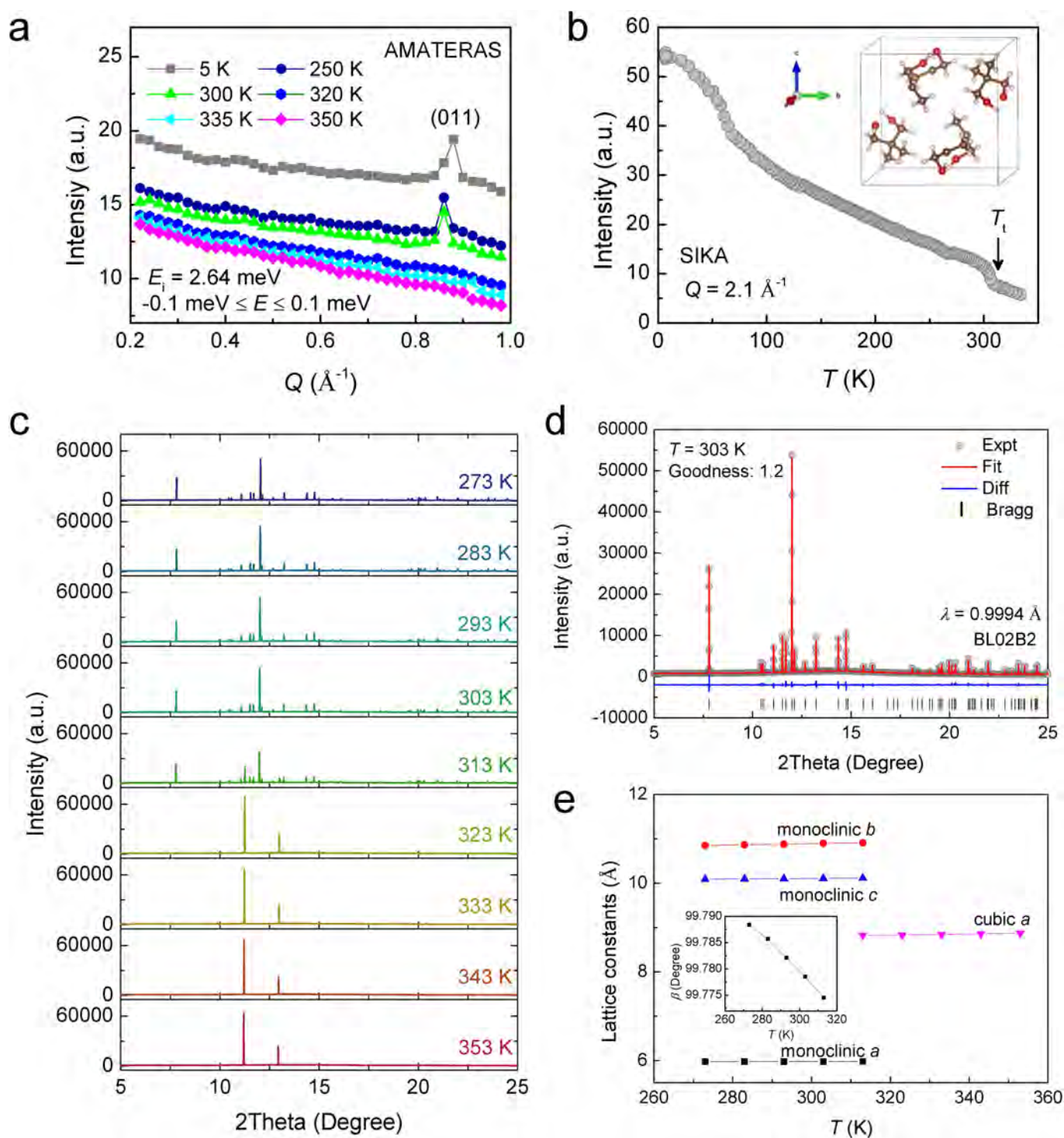
Extended Data Fig. 1 | Diffraction data and crystal structures of NPG. **a**, Integrated intensity at -0.1 meV $\leq E \leq 0.1$ meV across $T_t \approx 314$ K, obtained at AMATERAS. **b**, Elastic incoherent scattering intensity as a function of temperature at $Q = 2.1$ Å^{-1}, measured at SIKA. The inset shows the crystal structure of the monoclinic phase. **c**, Synchrotron XRD patterns of NPG in the temperature region 273–353 K, obtained at BL02B2 with a wavelength of 0.9994 Å. **d**, Rietveld refinement of the data at 303 K. Expt, experimental data; Fit, simulated pattern; Diff, difference between experimental and simulated results; Bragg, position of Bragg peaks; Goodness, χ^2. **e**, Temperature dependence of the lattice dimensions across the phase transition.
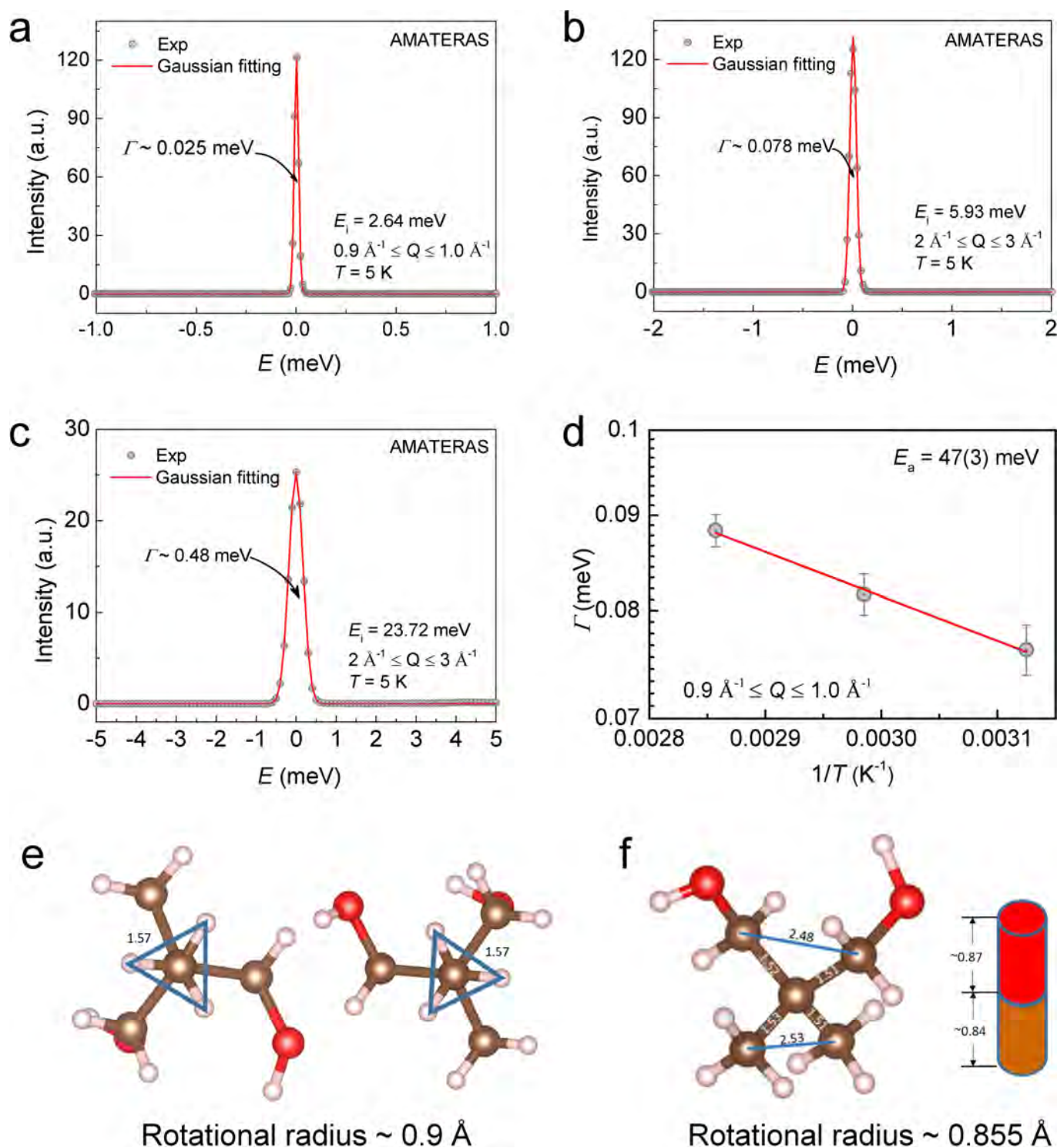
Extended Data Fig. 2 | QENS analysis. a–c, Energy resolution at different incident energies E_i. **d,** Activation energy (E_a) of the isotropic reorientational mode, obtained by fitting the temperature dependence of the experimental linewidth Γ. **e, f,** Simplified reorientational models. Brown, red and pink spheres represent carbon, oxygen and hydrogen atoms, respectively. Distances are given in ångströms. **e,** Triangles with side length of 1.57 Å indicate the configuration of hydrogen atoms in the methyl groups. The rotational radius of about 0.9 Å corresponds to the distance from the centre of the triangles to the hydrogen atoms. **f,** The distances between carbon atoms are labelled. The distance between the

central carbon atom and C(CH$_3$)–C(CH$_3$), which links the two carbon atoms of the methyl groups, is about 0.84 Å, and that between the central carbon atom and C(CH$_2$OH)–C(CH$_2$OH), which links the two carbon atoms of the hydroxymethyl groups, is about 0.87 Å. These two distances are shown schematically on the right, and their average value is 0.855 Å. This isotropic reorientation model with a rotational radius of 0.855 Å describes a complex reorientational mode consisting of a free rotational reorientation of the whole molecule with respect to an axis perpendicular to C(CH$_3$)–C(CH$_3$) and C(CH$_2$OH)–C(CH$_2$OH), and an isotropic rotational reorientation of this axis.
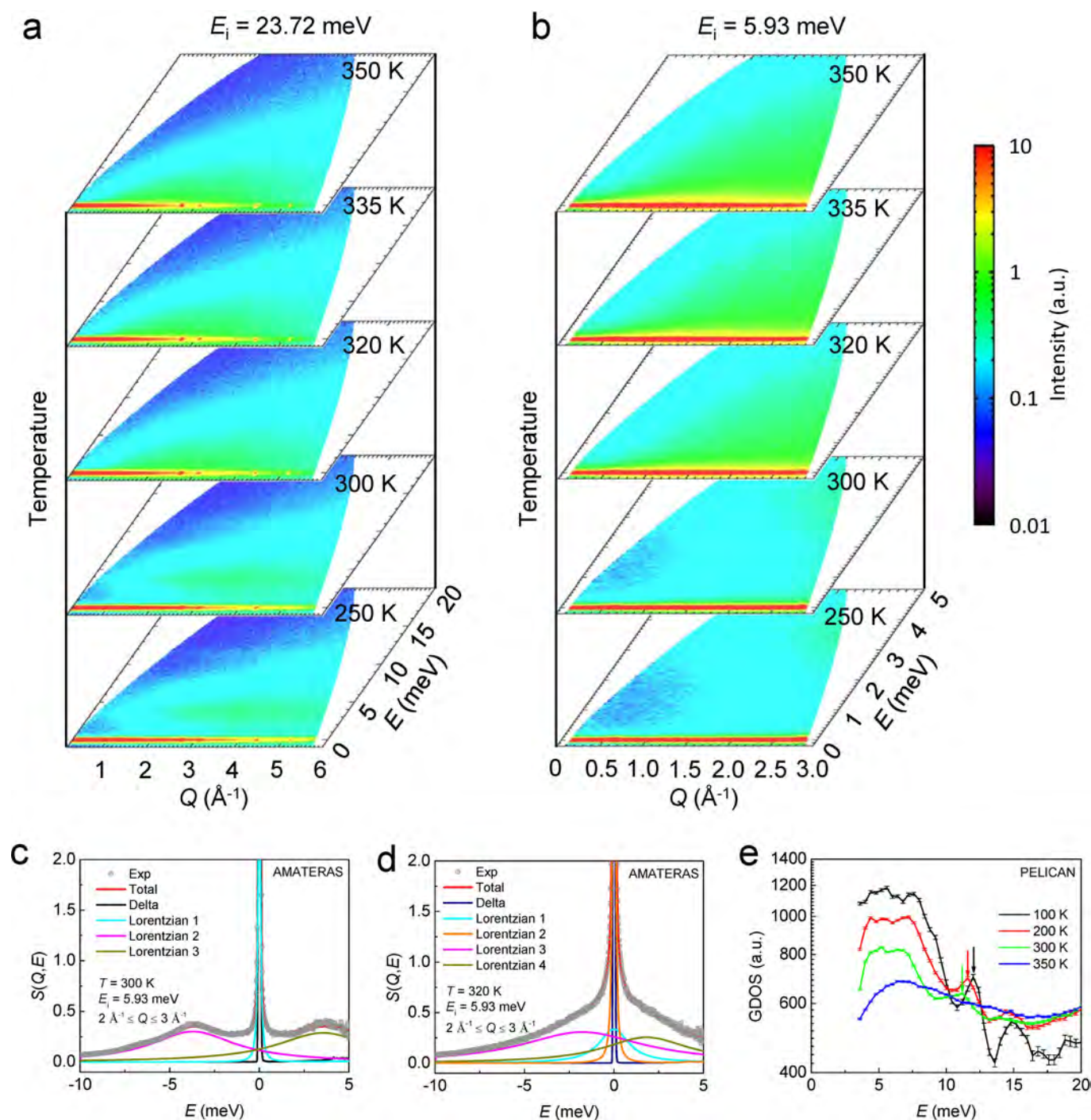
Extended Data Fig. 3 | INS data with higher E_i. a, **b**, $S(Q, E)$ obtained at AMATERAS with $E_i = 23.72$ meV (**a**) and $E_i = 5.93$ meV (**b**). **c**, **d**, Multi-component fit of $S(Q, E)$ data at 2 Å$^{-1} \le Q \le 3$ Å^{-1} with $E_i = 5.93$ meV at 300 K (**c**) and 320 K (**d**). **e**, General density of state (GDOS), measured at PELICAN. The arrows indicate the peak positions of the mode around 12.7 meV.
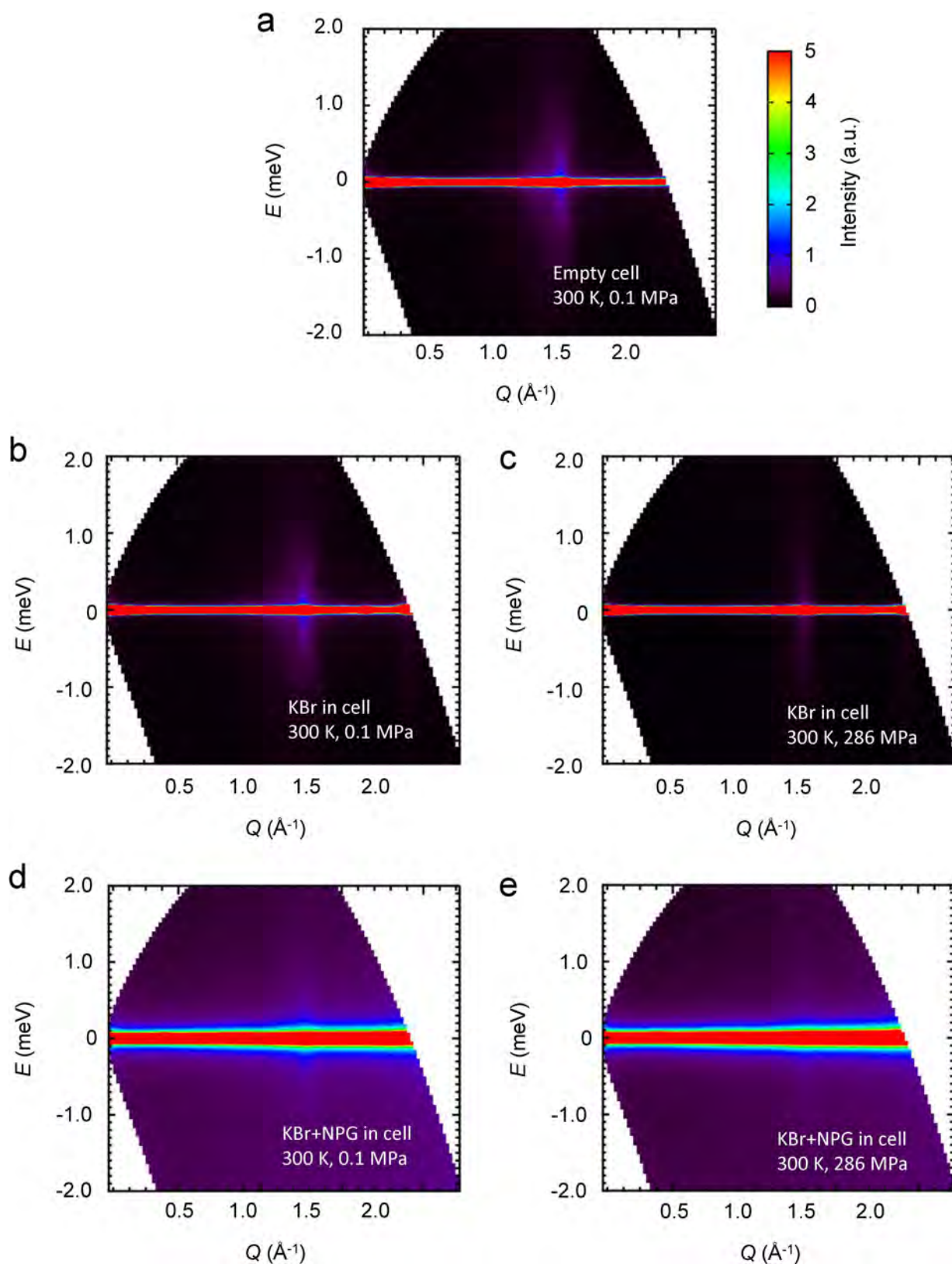
Extended Data Fig. 4 | QENS data. a–e, Data obtained with $E_i = 2.64$ meV at 300 K for an empty cell (**a**), the pressure-transmitting medium (KBr; **b**, **c**) and the sample (**d**, **e**). It can be seen that the inelastic signal at $Q = 1.3$ Å^{-1} originates from Teflon, whereas the pressure-transmitting medium KBr does not contribute much to the background.
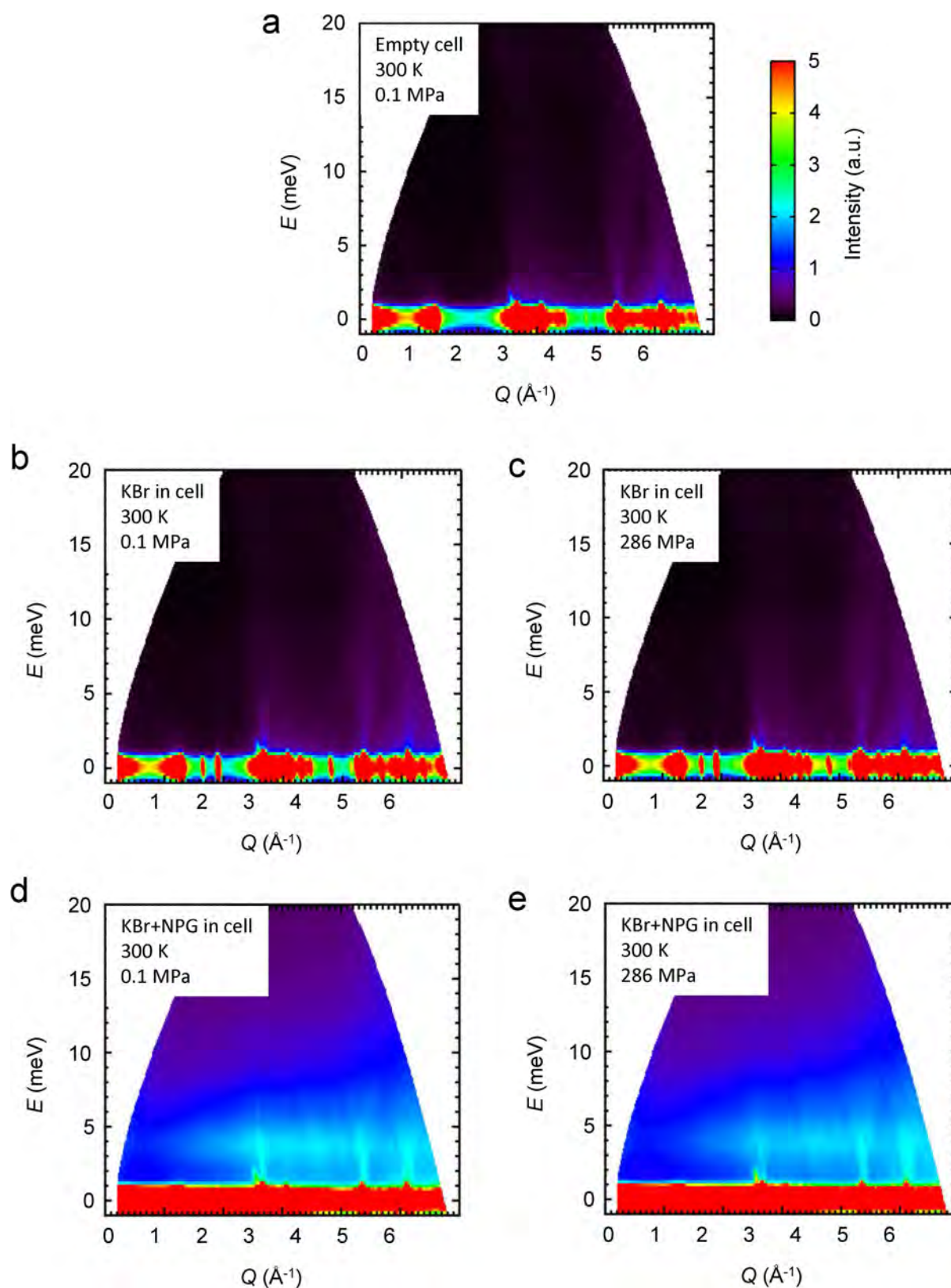
Extended Data Fig. 5 | INS data. a–e, Data obtained with $E_i = 23.72$ meV at 300 K for the empty cell (**a**), the pressure-transmitting medium (**b**, **c**) and the sample (**d**, **e**). The inelastic signals at about 2.7, 4.4 and 5.2 Å^{-1} are contributed by phonons from Teflon.
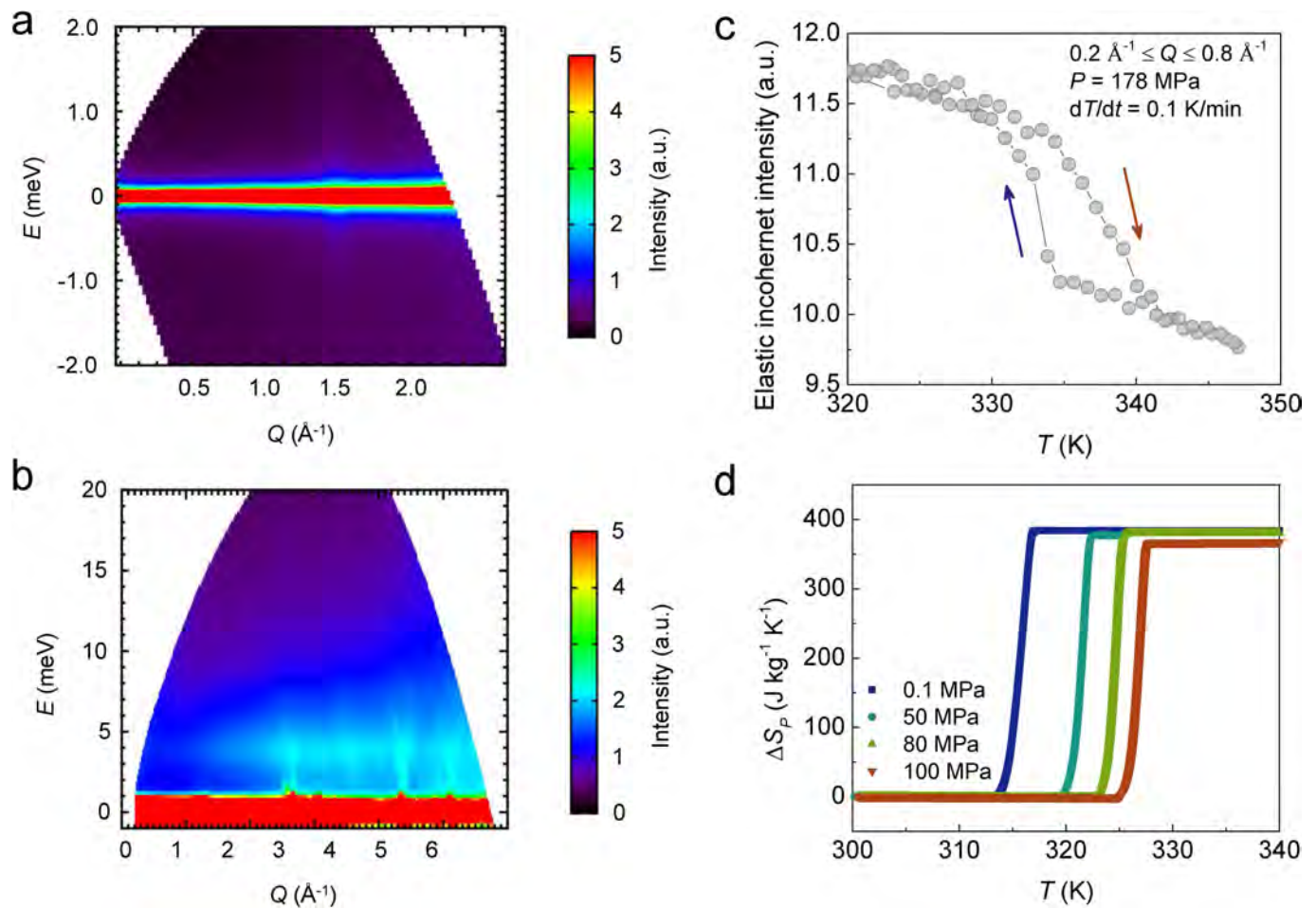
Extended Data Fig. 6 | Additional pressure-dependence data. a, $S(Q, E)$ at $E_i = 2.64$ meV, 178 MPa and 325 K. **b**, $S(Q, E)$ at $E_i = 23.72$ meV, 178 MPa and 325 K. **c**, Elastic incoherent scattering intensity integrated in 0.2 Å$^{-1} \leq Q \leq 0.8$ Å^{-1} with a ramping rate of 0.1 K min^{-1} at 178 MPa. The blue and red arrows indicate the cooling and warming processes, respectively. **d**, Entropy changes in NPG during heating for pressure changes from the ambient pressure (P_0) to the applied pressure ($P = 50$, 80 and 100 MPa), obtained using μDSC 7 EVO at Setaram, France.
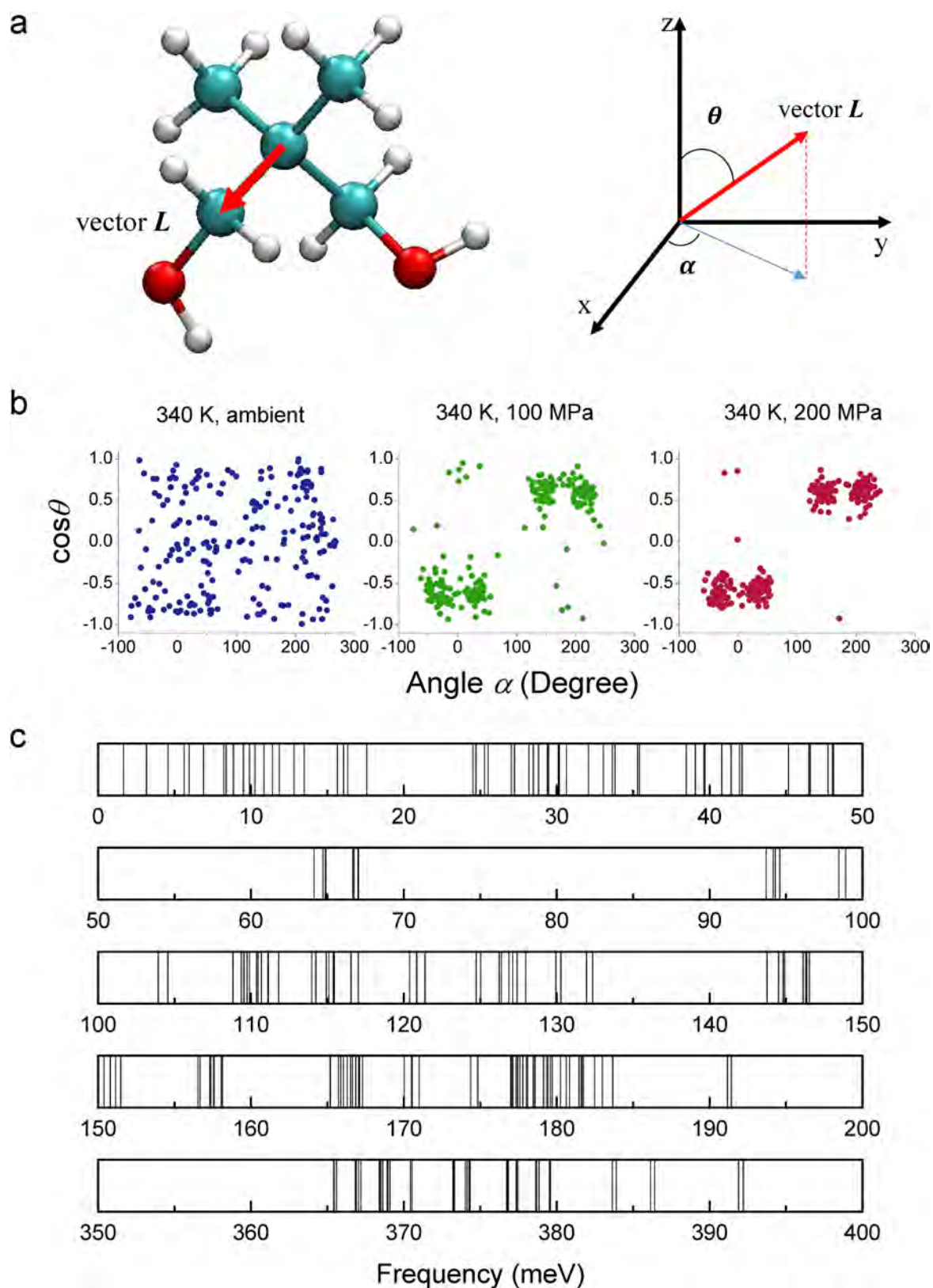
Extended Data Fig. 7 | Theoretical modelling. a, Atomic structure of the NPG molecule and its orientation, defined in three-dimensional space using angles α and θ in molecular dynamics simulations. Vector **L** points from the central carbon atom to a corner carbon atom of the molecule. **b**, Simulation results showing the distribution of the orientations of the molecules as a function of pressure at 340 K. It can be seen that a pressure of 100 MPa already effectively suppresses disorder. **c**, Full vibrational spectrum of NPG calculated by DFT. We note that there is a gap between 200 and 350 meV.

Extended Data Table 1 | Evaluation of entropy changes using the Clausius–Clapeyron relation on a few plastic crystals[12,13,14,20]

Plastic crystals	M (g mol⁻¹)	T_t (K)	dP/dT_t (MPa K⁻¹)	ΔV (cm³ mol⁻¹)	ΔV (m³ kg⁻¹)	ΔS (J kg⁻¹ K⁻¹)
NPG	104.15	313	7.5	5.4	5.18E-5	389
PG	120.15	354	9.4	6.3	5.24E-5	493
PE	136.15	461	8.3	10.5	7.71E-5	640
AMP	105.14	353	11.6	5.7	5.42E-5	629
TRIS	121.13	407	14.6	5.7	4.71E-5	687
MNP	119.12	308	10.7	4.5	3.78E-5	404
NMP	135.12	352	7.4	10.1	7.47E-5	553

M, mass; V, volume.

Extended Data Table 2 | Entropy changes of systems shown in Fig. 1c

Systems		Density (g cm^{-3})	Entropy changes	
			J kg^{-1} K^{-1}	J cm^{-3} K^{-1}
MCE	$Gd_5Si_2Ge_2$	7.54 [ref. 65]	19 [ref. 66]	0.14326
	$La(Fe,Co,Si)_{13}$	7.2 [ref. 67]	23.4 [ref. 3]	0.16848
	$MnGoGeB_{0.02}$	7.65 [ref. 68]	47.3 [ref. 27]	0.36184
ECE	PVDF-TrFE	1.78 [ref. 69]	55 [ref. 28]	0.0979
	$PbZr_{0.95}Ti_{0.05}O_3$	7.9 [ref. 70]	8 [ref. 71]	0.0632
	$BaTiO_3$	6.024 [ref. 72]	2.1 [ref. 73]	0.01265
eCE	TiNi	6.5 [ref. 74]	46 [ref. 29]	0.299
	$Cu_{68.1}Zn_{15.8}Al_{16.1}$	7.7 [ref. 5]	21 [ref. 75]	0.1617
	$Fe_{49}Rh_{51}$	9.8 [ref. 5]	7 [ref. 76]	0.0686
BCE	$(NH_4)_2SO_4$	1.7 [ref. 5]	60 [ref. 25]	0.102
	AgI	5.69 [ref. 77]	62 [ref. 9]	0.35278
	rubber	0.975 [ref. 78]	90 [ref. 10]	0.08776
	NPG	1.069 [ref. 30]	389 [this work]	0.41584
	AMP	1.211 [ref. 79]	629 [this work]	0.76172
	PG	1.15 [ref. 80]	493 [this work]	0.56695
	PE	1.435 [ref. 81]	640 [this work]	0.9184
	TRIS	1.335 [ref. 82]	687 [this work]	0.91714
	MNP	1.21 [ref. 83]	404 [this work]	0.48884
	NMP	1.315 [ref. 84]	553 [this work]	0.72719

The data are expressed both in J kg^{-1} K^{-1} and in J cm^{-3} K^{-1}, converted using the density data.

Extended Data Table 3 | Crystal structure information, determined by XRD measurements at 303 K and by DFT calculations

Lattice dimensions	XRD	DFT
a (Å)	5.97861(2)	5.963
b (Å)	10.89609(3)	10.375
c (Å)	10.10867(3)	9.806
β (°)	99.7786(3)	100.20